





RESEARCH ARTICLE OPEN ACCESS

# Performance Analysis of an Onboard PV System on a Demonstrator Light Commercial Vehicle in Hannover, Germany

<sup>1</sup>IMD 3, Photovoltaics, Forschungszentrum Jülich, Jülich, Germany | <sup>2</sup>Institute for Solar Energy Research Hamelin (ISFH), Emmerthal, Germany | <sup>3</sup>Energy Technology, Eindhoven University of Technology, Eindhoven, Netherlands

Correspondence: Neel Patel (n.patel@fz-juelich.de)

Received: 26 March 2024 | Revised: 17 December 2024 | Accepted: 22 January 2025

Funding: This work was supported by the Gauss Centre for Supercomputing eV and the German Ministry for Economic Affairs and Energy (FKZ 0324275).

Keywords: VIPV | Shading analysis | Irradiance modelling | Performance analysis

#### **ABSTRACT**

We present an analysis of the performance data of a monitored PV system onboard a light commercial electric vehicle during parking and driving conditions in the Hannover region of Germany. The PV system's nominal power is 2180  $W_p$  with flat silicon modules on the vehicle's roof, rear, left, and right sides and other electronic components needed to charge the vehicle's high-voltage (HV) battery. The analysis indicated that after 488.92 h of operation, the modules mounted on the vehicle roof produced 133.32 kWh of electricity during parking at the best possible orientation compared to 15.4, 30.67, and 22.99 kWh for the modules mounted on the rear, left, and right sides, respectively. During the trips, after 31.99 h of operation, 6.12, 0.68, 1.08, and 1.86 kWh of electricity were produced by the modules on the roof, rear, left, and right sides, respectively. The overall system efficiency was in the 60%–65% range. The aggregated usable electricity reaching the HV battery after multiple conversion stages generated by the system at the two parking locations was 129.39 kWh. PV electricity generated at the two parking locations enabled a range extension of approximately 530 km, which is 30% of the total distance driven during the measurement period between April and July 2021.

# 1 | Introduction

Electrification of one of the major sectors, road transport, has commenced to reduce their carbon emissions. However, the magnitude of the potential for carbon reduction depends on the electricity source. Efforts have been put into supplying this electricity demand from clean energy sources as much as possible. One of the solutions has been the use of stationery photovoltaic (PV) and battery storage systems [1]. Another proposal is to integrate PV modules into the vehicle to charge the battery directly. This approach of onboard vehicle PV has challenges such as limited surface area, weight, durability constraints, and the need

for special electronics for the vehicle interface, to name a few. The vehicle shape results in curved modules and self-shading, leading to losses. The losses due to the curvature can be significant, from 8% [2] to 25% [3]. Cell interconnection adaptation to the curvature can mitigate this problem [3]. Introducing the VIPV system brings additional weight to the car, and Patel et al. [4] defined the yield factor, allowing us to judge this impact. VIPV modules are exposed to much more significant partial shading situations, and this impact has been studied by Arun and Mohanrajan [5] using electrical loss simulations. The constraints are relatively relaxed for commercial vehicles, such as delivery vehicles, trucks, and busses, with larger surface areas

This is an open access article under the terms of the Creative Commons Attribution License, which permits use, distribution and reproduction in any medium, provided the original work is properly cited.

© 2025 The Author(s). Progress in Photovoltaics: Research and Applications published by John Wiley & Sons Ltd.

than passenger cars. For onboard vehicle PV to become a viable source of electricity, these constraints must be analyzed through simulations, experimentation, and prototyping. Eventually, these findings can trigger further optimization towards attractive amortization times for the PV system.

Activities to study various VIPV aspects have been ongoing in academia and industry. The temperature within vehicles exposed to direct sunlight can rise considerably, which may result in premature battery degradation. Kolhe et al. [6] collect temperature data for five July days in Scotland and use an 80W, PV module to manage the cabin heat temperature. Kouzelis [7] demonstrates that battery cooling reduces aging and annual grid charging frequency (by 23% in the Netherlands and 44% in Spain). Kouzelis [7] shows that VIPV can extend the battery life by up to 4.6 years, allowing 88,000 km of additional driving range. As batteries constitute a significant portion of the costs of electric vehicles, this may lead to a promising application of VIPV. The impact of climatic conditions is studied by Thiel et al. [8], where it was established that the power needed to drive electric vehicles on identical routes could vary by more than 44% between considered six climate regions.

One of the most essential aspects is understanding the potential irradiation available for such a PV application, where there is a higher probability of light getting blocked by various objects as the vehicle moves or is parked. Several groups studied VIPV potential through simulations [9-12]. Field data collection and simulation efforts have been ongoing at various locations to study the irradiation potential for onboard vehicle PV. Sovetkin et al. [13] collected irradiance and wind measurements from a single vehicle for 8 months in Germany. The citizen science project PV2Go [14] distributed 50 irradiance sensors among private car owners and commercial track vehicles in Germany. Araki et al. [12] and Ota et al. [15] collected year-long experimental irradiance measurements in Japan with a single vehicle using five sensors. Wetzel et al. [16] use three high-frequency pyranometers (up to 1 kHz) to record irradiation along a 21-km track in Hanover and study its impact on the MPP tracker design. Their findings indicate that irradiance changes predominately occur at frequencies below 1 Hz; however, changes with 100 Hz can occur in certain situations, often during sunny weather. De Jong and Ziar [11] and Sionti [17] measured the performance of a small PV system on a commercial boat in the Netherlands.

Wendeker et al. [18] describe the PV system installed on a passenger bus with measurement in Poland. The PV system consists of 22 solar PV panels of 2.88 kW $_{\rm P}$ , with VIPV providing up to 21% of the total electricity consumed during the best days. The analysis of the complete system and range extensions for commercial busses is also considered in Karoui et al. [19, 20], where for the average European case, assuming 30% shading losses, they report that VIPV provides an additional annual range of 3700 km.

Lade-PV project [21] reports a complete prototype of an electric truck with PV modules on the roof and necessary electronics to supply the PV electricity to the vehicle battery with 800V architecture. Peibst et al. [22] report a demonstrator light commercial vehicle with PV modules integrated into the vehicle body and necessary electronics to supply electricity to the vehicle battery

with 400-V architecture. Furthermore, products ranging from purpose-built PV-integrated cars to add-on kits for trucks and busses are under different stages of development [23–25].

This work is a continuation of a past paper [22] in which an energy flow analysis of the collected data for a single exemplary day was presented. Here, we present a more detailed and statistically sound analysis over a long period of 4 months from April to July 2021. The focus will be on individual components in the system, such as PV modules, MPPTs, low voltage (LV) buffer battery, DC-DC converter, high voltage (HV) vehicle traction battery, and the overall losses occurring in the system. This analysis provides an overview of how such an onboard vehicle system functions, what efficiencies can be expected from the system components, and how much PV-produced electricity is available for end use in the HV battery. The main results are visualized using a Sankey diagram with energy flows and losses occurring at each stage in the system. The shading losses visualized in the Sankey diagram are determined using simulations. Such a diagram provides insights into optimizing such a system for commercial deployment.

The paper is organized as follows: Section 2 presents the system and descriptions of the collected data. Section 3 describes shading analysis using irradiance simulations. Section 4 presents the complete system analysis, and Section 5 concludes the paper.

# 2 | Experimental

# 2.1 | System Description

The demonstrator vehicle was created by modifying a StreetScooter model "Work L," a light commercial electric vehicle used mainly by the Deutsche Post for mail delivery. Figures 1 and 2 show the finished demonstrator vehicle with flat PV modules on its rear boxed body and various sensors, which are highlighted. The vehicle consists of two experimental systems: (1) weather and location measurement system and (2) onboard PV system. Both systems measure various system parameters necessary for the system analysis. The description of the sensors used and parameters monitored by both systems are listed in Tables 1 and 2. The vehicle's gross weight is 2015.

A MicroAutoBox managed the data collection for both systems with different sampling rates for different components, which were downsampled to a uniform 1 Hz for this analysis. The peak power of the PV modules was 2180 W<sub>p</sub> with 875  $W_{\rm p}$  on the roof, 215  $W_{\rm p}$  on the rear side, and 545  $W_{\rm p}$  on the left and right sides. The PV modules occupied a total of 15 m<sup>2</sup>, whereas large parts of this area were left blank due to the constraints of full M2 wafer Si solar cells. When only considering the "essential" parts of the modules (cells, intercell spacing, interconnectors, etc.), 4.63, 1.2, 2.88, and 2.88 m<sup>2</sup> of the area on the roof, rear, left, and right sides of the vehicle are "PV active." The roof modules were individually connected to 5 separate MPPTs, and for the rear, left, and right sides, two modules in series were connected to a single MPPT tracker. A high-level onboard PV system schematic is shown in Figure 3, with a picture of the actual interconnection of all

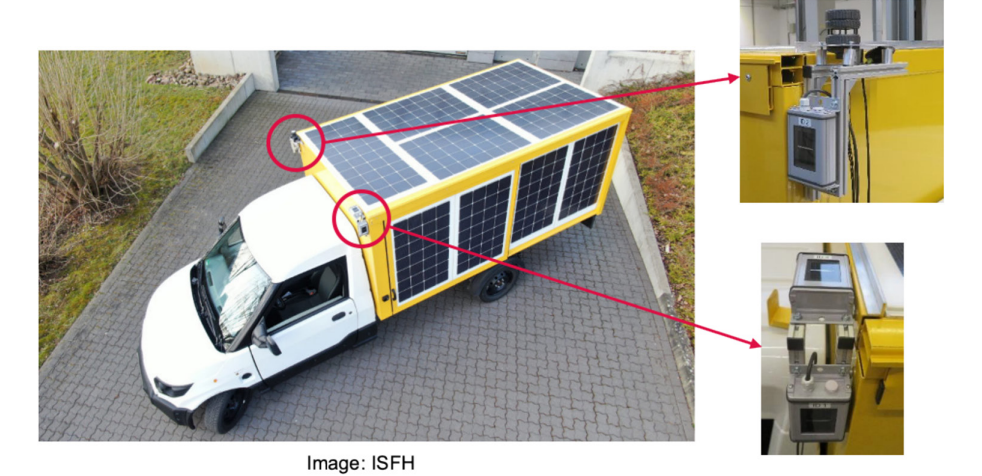


FIGURE 1 | StreetScooter vehicle with the flat PV modules visible on the roof and the left side. The irradiance sensors, as well as the acoustic wind sensor, are also highlighted.



**FIGURE 2** | Rear side flat PV modules visible on the prototype along with the irradiance sensor located near the bottom part (highlighted red) kg, with the weight of added PV and measurement systems being 320 kg. The weights of the individual components are noted in Table 2. For a similar commercial system, using the specific weight of flexible PV modules of  $2.2 \, \text{kg/m}^2$  [4] and the balance-of-system (MPPTs, DC-DC converters, wiring, and mounting structures) of  $10 \, \text{kg}$ , the total weight could be approximately  $35 \, \text{kg}$  (without the buffer battery architecture).

the electronic components shown in Figure 4. All the MPPTs were connected to the LV battery and the DC-DC converter. The onboard energy management algorithm, as described in [22], decided the power flow. Finally, the DC-DC converter supplied the power to the vehicle's HV battery. Parasitic and auxiliary power losses existed throughout the measurement period, which we could estimate from the collected data. The system description in Peibst et al. [22] complements the details provided here.

# 2.2 | Data Description

The vehicle was driven in a commuting pattern in the Hannover region of Germany. The commute started early morning (5:00 local time) from home (location is omitted here for privacy

**TABLE 1** | Weather and location measurement system specifications.

Sensor type	Description		
Irradiance	Mencke & Tegtmeyer, 3× Si-RS485TC-T-MB, 1× Si-RS485TC-2T-v-MB		
Wind speed and direction	FT205 from FT Technologies		
GPS	Adafruit 2324 GPS Hat for the Raspberry PI		
Magnetic compass	Adafruit magnetometer (LSM303)		

reasons) to the Institute for Solar Energy Research Hamelin (ISFH), an approximately 45-min trip; the vehicle remained parked there for a few hours and then returned home in the afternoon for the remainder of the daytime before taken inside for charging from the grid. This commute pattern was followed for most measurement days from April 2021 till December 2021 but not always. There were instances where data were available for trips and not for parking on a given day and vice versa. The duration of the trips and parking sessions also varied from day to day. The trip from home to ISFH in the morning was in the general direction of South to North and vice versa for the return trip. The vehicle's front side consistently faced North-West (330°) during parking at ISFH and home, so the PV modules on the rear side faced close to South.

During this commute pattern, data were continuously collected for all the sensors and PV system components. The quantities measured by the weather and location measurement systems are mentioned in Table 1. The onboard PV system current and voltages were measured for all the individual components on the input and output side. Temperature measurements were performed for the electronic components like the MPPTs, LV battery, DC-DC converter, and HV battery. Further, for both the batteries, the state of charge (SOC) was also measured continuously. All these weather, location, and system-related measurements

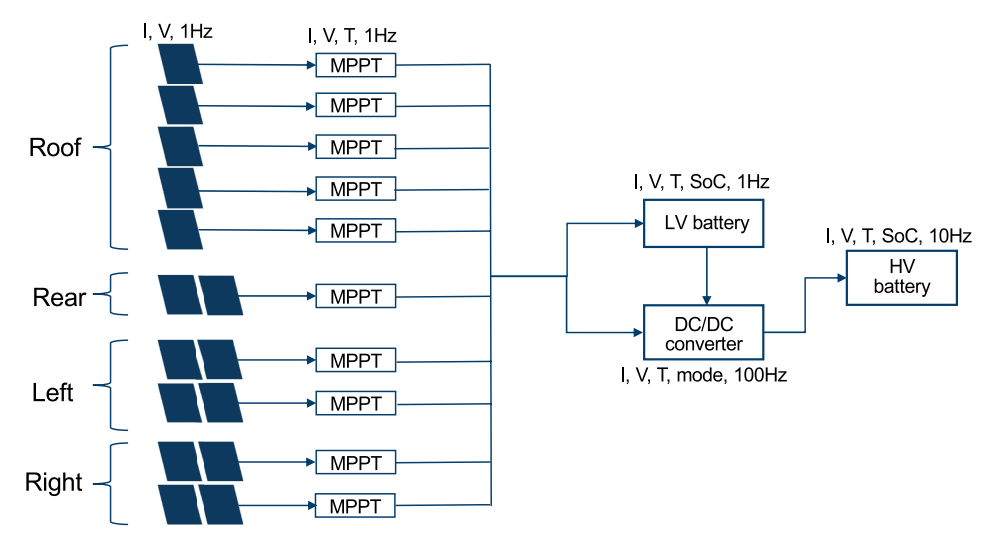


**FIGURE 3** | High-level schematic of the onboard PV system. The arrows show the power flow from the modules to MPPTS, the LV battery, the DC-DC converter, and the HV battery. The measured data are indicated on each component, where *I* is the current, *V* is the voltage, *T* is the temperature, *SoC* is the state of charge, and *mode* is the operation mode of the converter. The measurement frequency of each component is also indicated in Hz.

**TABLE 2** | Vehicle onboard PV system specifications.

Component	Specifications/description				
PV modules, roof	Glass/glass from a2-solar, monofacial, silicon heterojunction (SHJ) solar cells from Meyer- Burger Germany (full M2 wafers), Smart Wire Cell interconnection technology, 11.5 kg/m² 5 modules, essential area $4 \times 0.9  \text{m}^2 + 1.03  \text{m}^2$ $4 \times 170.1  \text{W}_{\text{p}}, 10.35  \text{kg}; 1 \times$ $194.4  \text{W}_{\text{p}}, 11.845  \text{kg}$				
PV modules, rear	See above, two modules with an essential area of $1.2  \text{m}^2$ in total, 215 W $_{\text{p}}$ , 13.8 kg				
PV modules, left	See above, four modules with an essential area of $0.72  \text{m}^2$ , $136.25  \text{W}_{\text{p}}$ , and $8.28  \text{kg}$ each				
PV modules, right	See above, four modules with an essential area of $0.72  \text{m}^2$ , $136.25  \text{W}_{\text{p}}$ , and $8.28  \text{kg}$ each				
MPPTs	10 MPPTs from Vitesco, 12V, (weight not available)				
LV battery	Varta G14 12 V 850 A 95 Ah, 26.4 kg				
DC-DC converter	Prototype from Vitesco, buck-boost converter from 12V to 400V, 2.85kg				
HV battery	StreetScooter vehicle battery, 40 kWh				

help us analyze this complex system on a high level in terms of energy flow analysis and also on a component level to help us determine the performance and efficiency of each component in the system chain and hence allow us to determine the chain efficiency of such a system.



**FIGURE 4** | Components of the PV system: 10 MPPTs, LV battery, DC-DC converter, cooling system, and others.

The data collection happened in separate text files for different system components for different days, which were synchronized using timestamps to form a complete dataset. This dataset was further filtered and processed to perform our analysis. Instances with GPS location errors and outliers encountered in various measured quantities were removed. After this cleaning process, it was determined that the system had a malfunction where the DC-DC converter stopped working for a considerable period of the entire duration. This malfunction affected the collected data for the rest of the onboard PV system but not the weather and location data. For such an experimental setup, malfunctions are expected, providing a learning opportunity to further optimize the system architecture and performance. After removing all the data affected by the malfunction, we were left with around 50% of the data, for a period between April and July 2021, usable for the overall system analysis, as mentioned in Section 4. This amounted to around 1.8 million complete measurements. However, as mentioned earlier, the malfunction did not affect the weather and location data, and the complete data were used to validate the

irradiance simulation model mentioned in Section 3. The data used for overall system analysis were further separated into the different parking locations and the trips for simplification reasons, and power flow through each component was calculated along with the aggregated power for each vehicle side (roof, rear, left, and right). The measurement period covered 80 parking sessions, totaling around 488.92h of operation. It also included 56 trips covering around 1750km of distance and 31.99h of operation.

# 3 | Irradiance Simulation

We augment the collected irradiance measurements with the simulation data. We obtain high-resolution topography and satellite-based atmospheric irradiation data and simulate the irradiation for the four vehicle sensors for the recorded vehicle time and locations. In Sovetkin et al. [13], we have already demonstrated and verified our simulation approach on the different VIPV measurement campaigns. However, Sovetkin et al. [13] performed a simulation for the trip data, and this paper also confirms the simulation model for the parking states.

We obtain unstructured aerial-based LIDAR data for the topography data and resample it to generate Digital Elevation Model (DEM) structured rasters. For every region of fixed size  $25 \times 25 \, \mathrm{cm}^2$ , we evaluate the maximum and minimum statistics of the point's elevation in that area. These so-called max and min statistics allow accessing the impact of vegetation. Figure 5 shows examples of the min and max DEM, where most vegetation is absent in the min-statistic raster. The white points in Figure 5 indicate the recorded locations of the vehicle during the trips.

We use Copernicus [26], a satellite-based atmospheric data service for the atmospheric irradiance data. It provides surface level Global Horizon Irradiance (GHI) and Diffused Horizon Irradiance (DHI) model values that consider the cloud coverage with a spatial resolution of approximately 5 km and a temporal resolution of about 10 min.

Our irradiance model implementation is similar to the one described by Fu and Rich [27]. We divide the sky dome into patches and assign an irradiance value for each patch according to the

Perez model [28], computed for the given GHI and DHI values. Nonisotropic sky incorporates different weather conditions, allowing a more accurate diffused light sky model. However, that model still neglects the cloud distribution and related effects.

The sky is projected on a surface with a given position and orientation, yielding the plane of array irradiance,  $I_{\rm PoA}$ , for each observation point. The  $I_{\rm PoA}$  consists of several components:

$$I_{\text{PoA}} := I_{\text{direct}} + I_{\text{diffused}} + I_{\text{ground}},$$
 (1)

where  $I_{\rm direct}$  is the direct light from the Sun,  $I_{\rm diffused}$  is the diffused light, and  $I_{\rm ground}$  is the light from the ground. The  $I_{\rm direct}$  is nonzero when the Sun is visible to the observer and is determined using observer orientation, Sun position, and the topography around the observer. The  $I_{\rm diffused}$  light consists of all visible sky patches and results from the sky model. The ground component  $I_{\rm ground}$  has a simplified model of the light reflected from the ground. We take the light from sky patches obstructed by the topography and scale the resulting value with the albedo parameter [0,1]. The simplified approach is similar to the ones used in open-source models [29,30] and a trade-off compared to computationally intensive methods such as ray-tracing.

Our simulations modeled the sky with 49,537 sky patches and 768 horizon elements. At least 500 m of topography data for each simulation point is guaranteed to be available in each direction. The usual value of albedo in the urban environment is in the range of 0.14 to 0.22; we assume an average value of 0.2 throughout the simulations [31]. Table 3 depicts the simulation, where we integrate irradiance over time and normalize data according to the data duration (trips, 31.99 h; Parking 1, 106.7 h; and Parking 2, 382.22 h). The simulation errors are lower for integrated irradiance as seen in Table 3. However, simulation errors as high as  $150 \, \text{W/m}^2$  (RMSE) can be observed [32]. The main source of errors in instantaneous irradiance predictions is the resolution of satellite weather data [33] (spatial resolution of  $5 \times 5 \, \text{km}$  and temporal resolution of  $10 \, \text{min}$ , interpolated to  $1 \, \text{min}$ ).

Our implementation of the above-described simulation pipeline is available as an open-source C library SSDP [34]. There, a user may specify a list of geo-raster data to describe the topography; provide time, GHI, and DHI values; select the



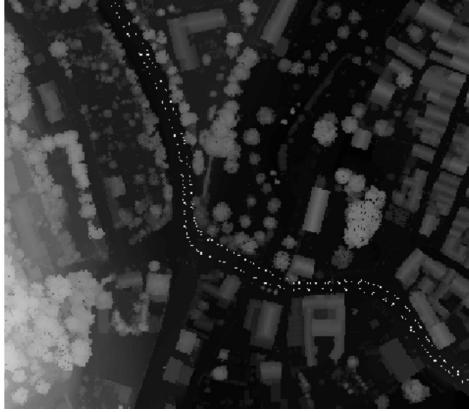


FIGURE 5 | Example of min (left) and max (right) LIDAR-based DEM. White points indicate recorded GPS vehicle locations.

**TABLE 3** | Irradiation (kWh/m²/24h) computed all available trips and parking locations. The values in square brackets beside the measured irradiation values are the relative % values of the rear, left, and right sides with respect to roof values. The values in square brackets in the remaining columns are the % simulation irradiation losses (error) compared to measured irradiation.

Locations	Sensor	Measured	Max-topo	Min-topo	No topo
Trips	Roof	5.93 [100]	5.74 [3.2]	6.68 [12.65]	7.08 [19.39]
	Rear	1.51 [25.46]	1.30 [13.91]	1.87 [23.84]	2.33 [54.3]
	Left	1.70 [28.66]	1.70 [0]	2.12 [24.71]	2.52 [48.24]
	Right	2.29 [38.61]	2.12 [7.42]	2.88 [25.76]	3.57 [55.9]
Parking 1	Roof	8.34 [100]	7.79 [6.59]	8.01 [3.96]	8.63 [3.48]
	Rear	3.99 [47.84]	3.87 [3.01]	4.5 [12.78]	4.91 [23.06]
	Left	1.65 [19.78]	1.96 [18.79]	2.17 [31.52]	2.70 [63.64]
	Right	7.13 [85.49]	6.16 [13.6]	6.59 [7.57]	7.41 [3.93]
Parking 2	Roof	8.35 [100]	8.07 [3.35]	9.16 [9.7]	10.11 [21.08]
	Rear	3.89 [46.58]	3.59 [7.71]	4.18 [7.46]	5.78 [48.59]
	Left	4.10 [49.10]	3.95 [3.66]	4.38 [6.83]	5.89 [43.66]
	Right	1.94 [23.23]	1.87 [3.61]	2.86 [47.42]	4.22 [117.53]

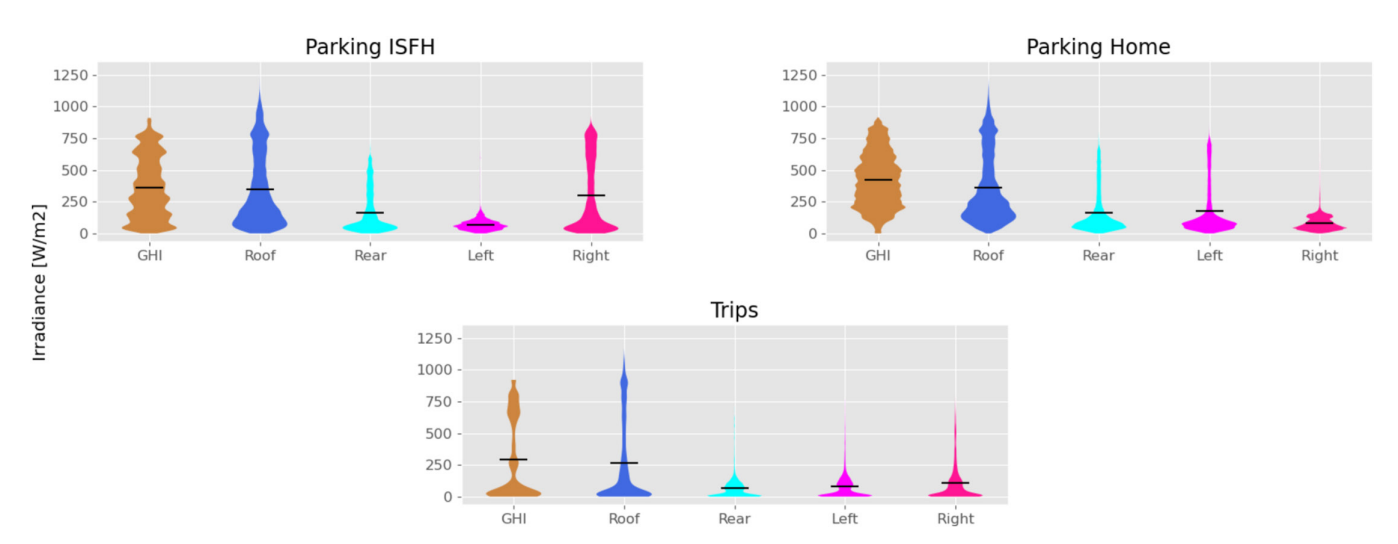


FIGURE 6 | The irradiance profile on various sides of the vehicle during parking at ISFH, home, and trips are visible as violin plots, with black horizontal lines showing the mean. GHI obtained from satellite sources is also appended for the respective location and time.

vehicle's three-dimensional positions; and perform the irradiance simulations.

## 4 | Results

The collected data were analyzed to estimate the performance of individual components and overall system performance. The power flowing through each component was integrated to get an energy number for individual parking sessions and trips. Each component's input and output energy flows were calculated, and their efficiencies were calculated as their ratio. Auxiliary power consumption and parasitic losses were estimated by accounting for energy input and output flows. In the following subsections, measured quantities for each component are visualized, along with losses occurring in each and their aggregated efficiencies.

# 4.1 | Irradiance and Shading Losses

Measured irradiance for the instances where all system data are available (i.e., without DC-DC malfunction) is visualized in Figure 6. The data are separated for the two parking locations and the trips. Measured irradiance in W/m² on the roof, rear, left, and right side is shown along with GHI from the CAMS data service [33]. The violin plots show the data's minimum and maximum value (extremities), and the distribution and mean are shown by the black horizontal line. The roof receives the highest irradiance at parking locations and during trips. While parking at ISFH, the right side receives more light than the left side, and during parking at home, the left side receives more light than the right due to the time of day and vehicle orientation. The vehicle's front side faces North-West at both locations, but at ISFH, the parking is in the morning

when the Sun rises, and at home, the Sun is setting, creating such irradiance profiles. The rear side has a similar irradiance profile at both parking locations, as the vehicle orientation is almost identical. During the driving phase, since the vehicle orientation continuously varies relative to the Sun, and due to obstruction from surrounding objects, the rear, left, and right sides receive relatively less irradiance.

#### 4.2 | Module Performance

Module power output aggregated for the individual sides of the vehicle is visualized in Figure 7. The peak power capacities are 875, 215, 545, and 545  $W_{\rm p}$  for the roof, rear, left, and right sides, respectively. The module outputs are correlated with the irradiance and follow the same pattern. The roof produces relatively more power at all locations. While parking at ISFH, the right side produces relatively more power, whereas the left side produces more power while parking at home. One interesting thing to note is that at the ISFH parking location because the right side is Sun-facing and two modules are connected in series to an

individual MPPT; the produced power is higher than the rating of the MPPT and is clipped, as seen by the flat-top shape of the violin plot.

Individual module power output on each of the sides is shown in Figure 8. The module power outputs on the same side have, on average, the same output with minor variations, which can be attributed to slight differences in the modules due to manufacturing defects and, to some extent, partial shading. On the roof, four modules, depicted by the first four violin plots, are the same size of  $0.9\,\mathrm{m}^2$ , and the last one is larger at  $1.03\,\mathrm{m}^2$ . The power output of the larger module is slightly higher. Two modules on the left and right sides are connected in series, with a combined area of  $1.44\,\mathrm{m}^2$ , but still produce less power due to nonoptimal tilt and orientation.

### 4.3 | MPPT Performance

The MPPT efficiencies, that is, the ratio of the output of MPPTs to the output of the modules, are shown in Figure 9

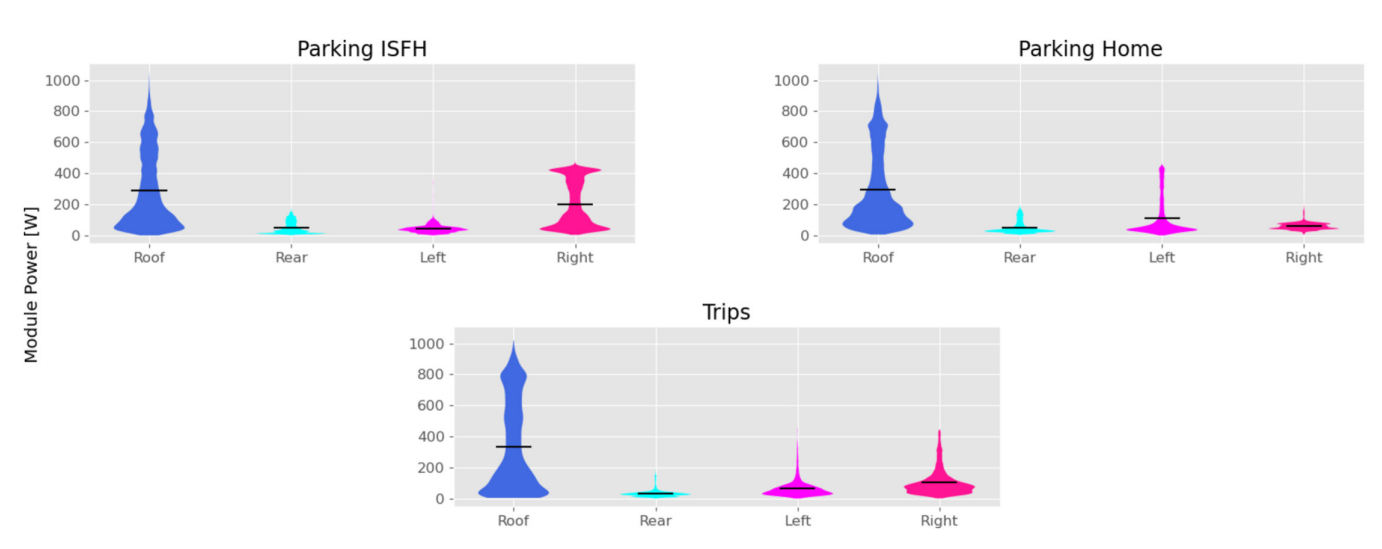
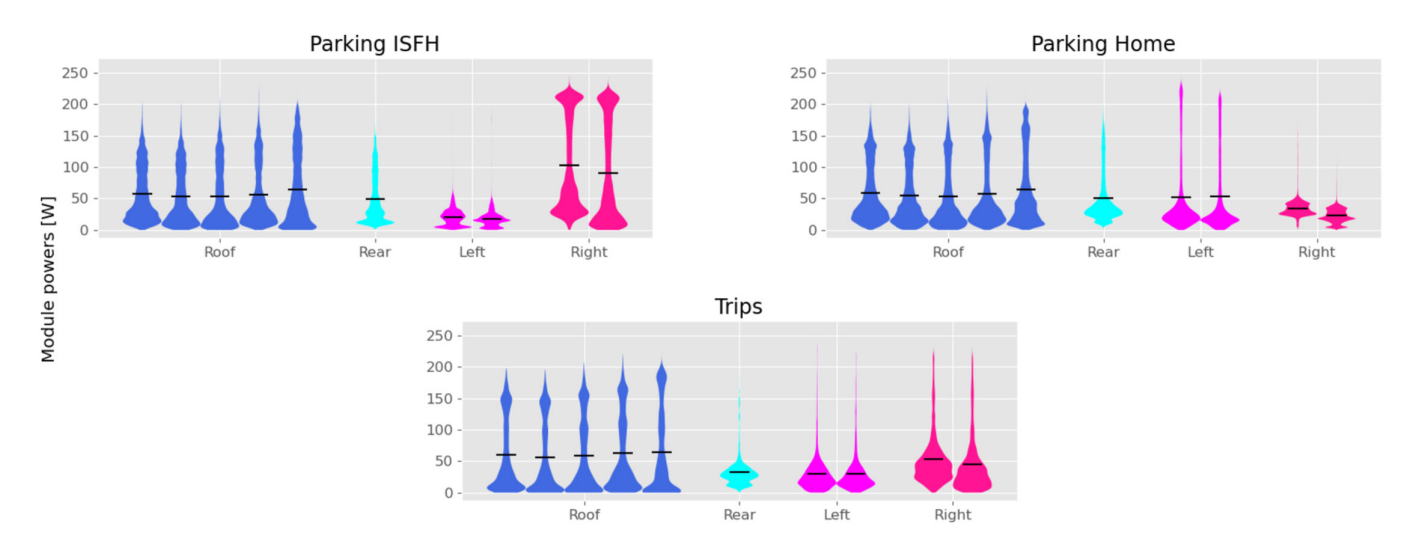
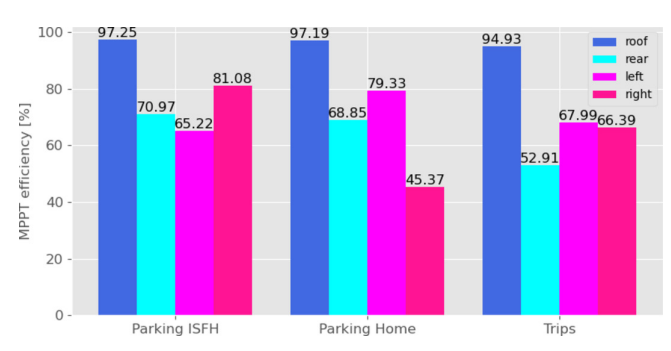


FIGURE 7 | The aggregated power output of each side is visualized as violin plots for the parking at ISFH, home, and trips.



**FIGURE 8** | Power output of individual modules visualized as violin plots. The power output of the modules on the rear, left, and right sides is a combined power of two modules connected in series.



**FIGURE 9** | Aggregated efficiencies of MPPTs connected to modules on each vehicle surface. Efficiencies are further separately shown for the parking at ISFH, home, and trips.

for aggregated modules on each side separated for the parking locations and the trips. The efficiency of the MPPTs connected to the roof modules is consistently higher even when the vehicle moves during the trips. However, the efficiencies are low for MPPTs connected to modules on the rear, left, and right sides with low light conditions as the MPPT works at lower capacities. This can be especially seen for the low light facing sides (due to vehicle orientation), for example, the left side while parking at ISFH and the right side while parking at home. For the rear, left, and right sides, two modules are connected to an individual MPPT, leading to consistently lower efficiencies than the roof, where each module is connected to an individual MPPT. Further, highly fluctuating irradiance due to partial and dynamic shading could cause lower

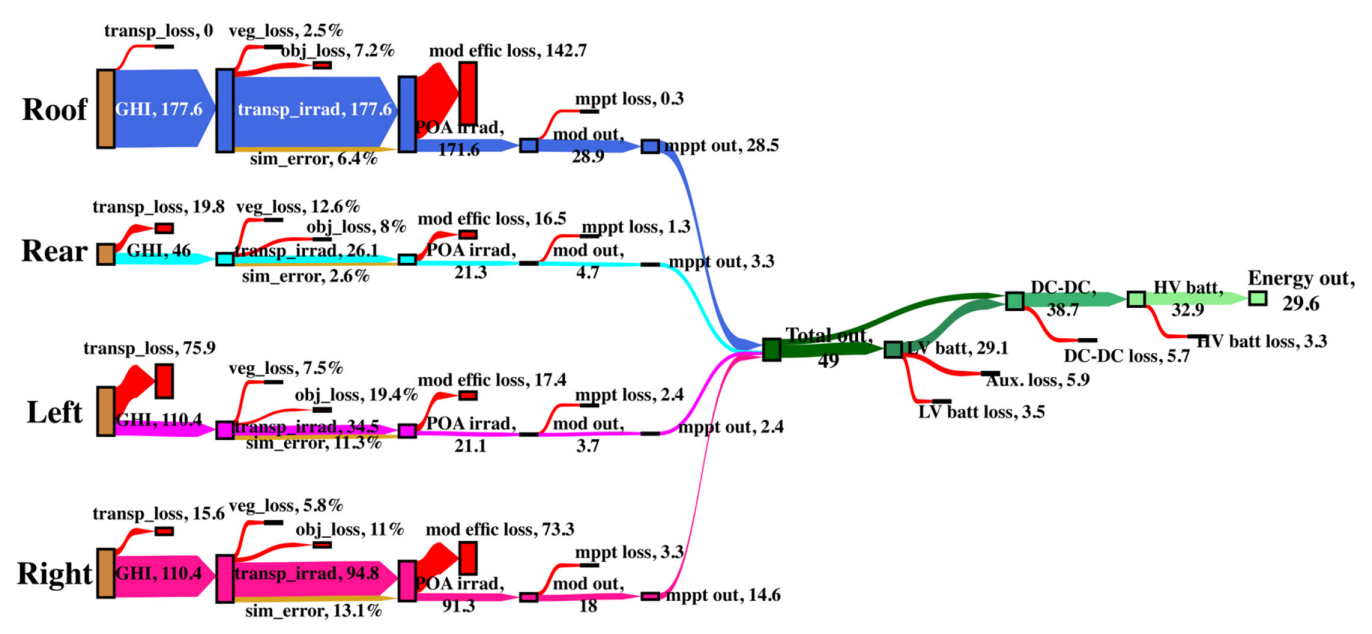


**FIGURE 10** | Energy flow Sankey diagram for aggregated parking data at ISFH. The energy flow numbers are mentioned in kWh except for the simulated shading losses and simulation error, which are in %.

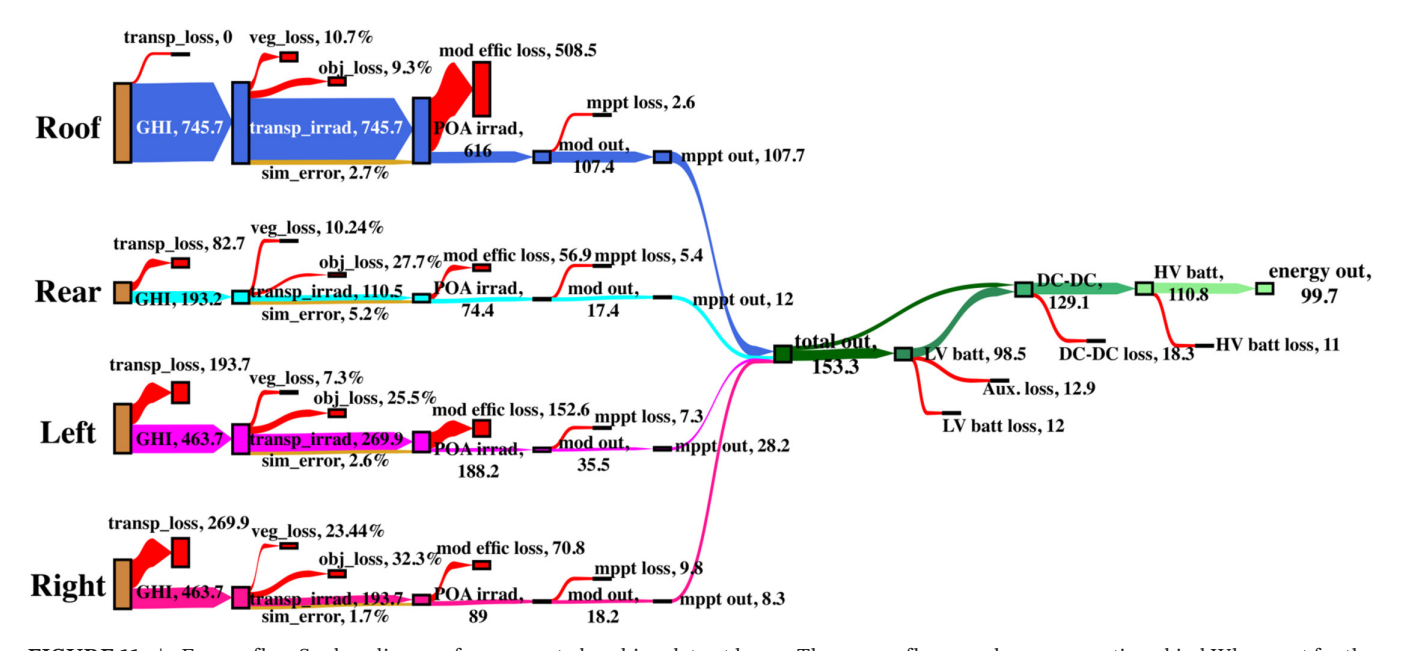


**FIGURE 11** | Energy flow Sankey diagram for aggregated parking data at home. The energy flow numbers are mentioned in kWh except for the simulated shading losses and simulation error, which are in %.

efficiencies for the rear, left, and right sides, along with the reasons mentioned earlier.

# 4.4 | DC-DC Converter

The DC-DC converter boosts the LV battery discharge voltage from 10–12 to 400 V to match the 400-V architecture of the vehicle traction battery. The current on the LV side of the DC-DC converter is in the 175 A range, which is converted to around 5 A on the HV side of the converter. The high current accepted on the LV side makes it necessary to actively cool the converter with the cooling system visible as the pink fluid in a bottle in Figure 4. The efficiency of the DC-DC converter, that is, the ratio of HV side output and LV side output, is 90.25%, 90.52%, and 89.81%, respectively, for parking at ISFH, home, and trips, respectively. Because the DC-DC converter is independent of the variability of weather due to the presence of the LV buffer battery, the efficiency is consistently the same at around 90% for parking and trips.

# 4.5 | Overall System Performance

The system's overall energy flow in and out of every component during the measurement period is visualized as a Sankey diagram, as shown in Figures 10–12. Each node in the diagram represents a component with the input/output arrows representing the flows, and the arrow's thickness is proportionate to the flow value represented. Each system component (node) is uniquely color-coded, with red representing losses occurring at every stage. Starting from the left side of the diagram, we have global horizontal irradiation for the available surface areas of the roof, rear, left, and right sides. GHI is followed by the simulated transposed irradiation, shading losses, measured plane of array irradiation, module energy output, MPPT conversion, LV battery, DC-DC converter, and usable energy to the HV battery. The shading losses are simulated, as described in Section 3, and prone to error due to changes in the environment in which the

vehicle moves and also due to the errors in the satellite input data. These simulation errors are also highlighted in the Sankey diagram. Losses are represented for individual components. The energy transfer from MPPT to the DC-DC converter happens in two ways; when the DC-DC converter is in standby mode, all the output from MPPTs charges the LV battery, but when the DC-DC converter is functional, the LV battery is discharging, and the MPPTs directly feed to the DC-DC converter. This operation is shown as two separate arrows from the MPPT to the LV battery and the DC-DC converter. Furthermore, there is auxiliary power consumption to run the system cooling and other datalogging equipment supplied by the LV battery. Battery charging/ discharging losses are also visualized for the LV and HV battery. However, for the HV battery, there is extra consumption during the parking phase as the ignition switch is on for the measurements to happen. This extra consumption from the HV battery is present only due to the experimental nature of this system and should be easily avoided for commercial systems.

Figures 10 and 11 show the Sankey diagrams for the system energy flow at the ISFH and home parking locations, respectively. The parking duration was around 106.7 and 382.22h for the ISFH and home parking, respectively. The global horizontal irradiation (GHI) values for the different vehicle surfaces are visible, with the combined irradiation being 444.68 kWh and 1866.41 kWh, respectively (these values were derived from the satellite data taken from the CAMS service). After accounting for shading, due to vegetation and other surrounding objects, and array orientation, the combined plane of array (POA) irradiation was 305.5 and 967.62 kWh, respectively. The combined module conversion efficiency for both parking locations was around 18.12% (ISFH) and 18.41% (home), with the efficiency for each side inferable from the values shown in the diagram. Due to the parking orientation, as mentioned earlier, the right side is Sun-facing and has a higher output for parking at ISFH, and the left side is Sun-facing and has a higher output for the home parking. A combined total of 49.06 kWh (ISFH) and 153.32 kWh (home) of energy is available after the MPPT conversion stage, out of which 29.16 kWh (ISFH) and 98.57 kWh (home) charge the LV

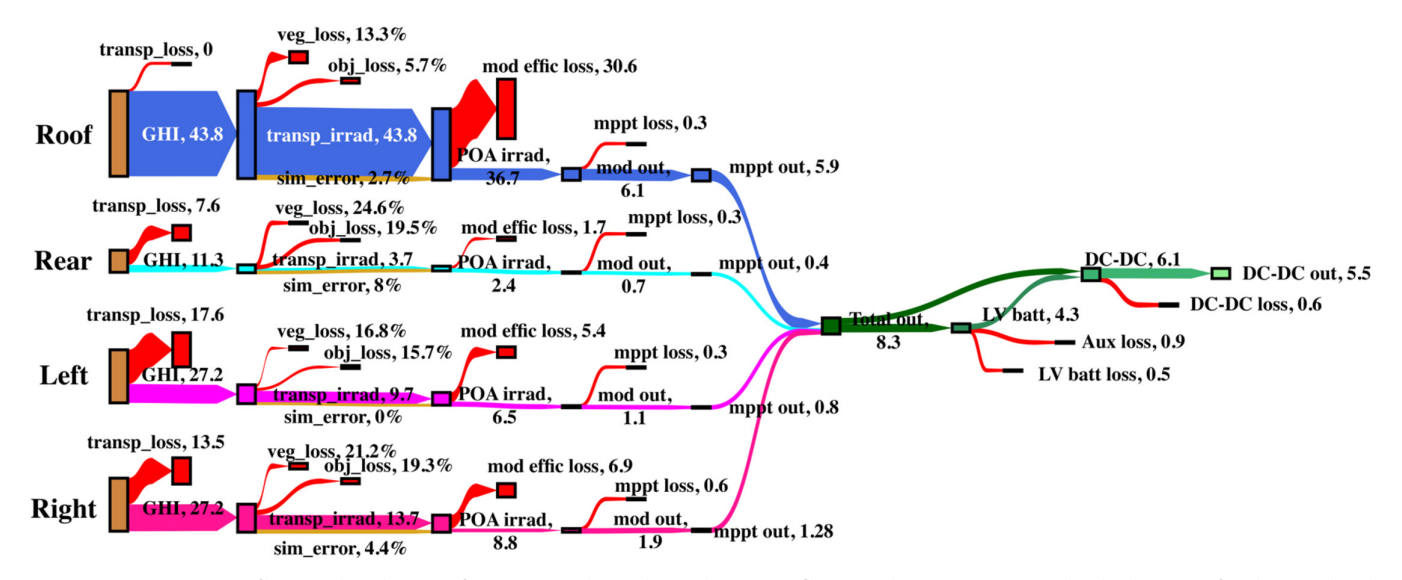


**FIGURE 12** | Energy flow Sankey diagram for aggregated trip data. The energy flow numbers are mentioned in kWh except for the simulated shading losses and simulation error, which are in %.

battery, 19.9 kWh (ISFH) and 54.75 kWh (home) are transferred directly to the DC-DC converter, and 5.96 kWh (ISFH) and 12.92 kWh (home) are the auxiliary consumption loss of the system. The LV side of the DC-DC converter receives 38.73 kWh (ISFH) and 129.18 kWh (home), which is sent to the HV battery. After considering the losses in the HV battery, the usable energy for traction is 29.65 kWh (ISFH) and 99.74 kWh (home).

Figure 12 shows the energy flow Sankey diagram for the driving phase for 31.99 h of operation. The combined GHI received on the vehicle surfaces is 109.5 kWh with the transposed irradiation being 70.9 kWh. The shading losses (from surrounding objects and vegetation) amount to 16.5 kWh leading to a combined POA irradiation of 54.4 kWh, which is available for the PV modules, which produce 9.8 kWh of electricity at an 18.01% conversion efficiency. After the MPPT conversion stage, 8.3 kWh of electricity is available for the further stages out of which 4.3 kWh charges the LV battery and 4 kWh is directly provided to the DC-DC converter. After accounting for 0.5 and 0.9 kWh of LV battery and auxiliary losses, respectively, 6.1 kWh of electricity is available at the low voltage side of the DC-DC converter. The final output of the DC-DC converter is 5.5 kWh, which is transferred to the HV battery of the vehicle during the driving phase. Because the HV battery is simultaneously discharging at several kilowatts and charging through the PV system during the driving phase, it was not possible to calculate the usable energy delivered from a single power time series of the HV battery and is not shown in the Sankey diagram.

The overall system efficiency considering multiple power conversion stages (MPPT & DC-DC), battery charging/discharging losses, and auxiliary losses is 60.44% for ISFH parking, 65.05% for home parking, and 66.26% for trips (the HV battery stage efficiency is excluded for the driving phase). The system efficiency at the home parking location is around 5% higher than the ISFH parking location. The losses in the LV battery, DC-DC, and the HV battery stage are decoupled from the weather conditions and are almost the same percentage values for both locations at around 12%, 14%, and 10%, respectively. However, the MPPT efficiencies and the auxiliary losses, which partly correlate with the cooling load and are dependent on weather conditions, are responsible for the differences in the overall system efficiencies at the two parking locations. The consistent losses occurring in the remaining system stages at the two different parking locations, namely, the LV battery, DC-DC converter, and the HV battery, highlight the losses that can be expected from such components. It is important to note that the HV battery losses reported here are relatively higher due to the unwanted consumptions occurring due to the vehicle ignition switch being on to enable the measurements. This problem can be rectified in the commercial iteration of such a PV system, making those losses relatively lower. It has been reported that the commercial VIPV systems on passenger cars and busses could have a combined system efficiency of 86% in the case of a buffer battery (12 or 48 V) architecture and 91% in the case of a direct coupling of the VIPV system with the vehicle HV battery [19, 20]. The efficiencies reported in the literature are apparently for an ideal case commercial product in the distant future. The system efficiency reported in this manuscript is for an experimental system, which has a lot of potential for optimizations to take it closer to the ideal values reported in the literature. For the

experimental system, useful energy generation of approximately  $38.8\,\mathrm{kWh}$  (ISFH) and  $123.6\,\mathrm{kWh}$  (home) would be possible if the energy consumptions occurring due to the measurement system and the ignition switch being on were removed. These energy generation estimates without the losses in the measurement system would translate to a system efficiency of 79.18% (ISFH) and 80.62% (home).

The range extension made possible by the PV-produced energy was estimated. First off, the average consumption of the vehicle was calculated based on the trip data collected for the HV battery. The HV battery power time series comprises the power flow to the electric motor, regenerative braking, and the PV electricity fed during the trips. We integrated this power flow for the number of trips we measured. This energy value gives energy consumption for a given trip, which is already adjusted for the PV energy injected during the trip. We calculated the consumption per kilometer for all the trips and estimated the average for all the trip data to be 244Wh/km. This calculated energy consumption already accounts for the PV electricity injected into the HV battery during the driving phase. From the Sankey diagrams for the two parking locations, we can estimate that 129.39 kWh of electricity was fed to the HV battery. Using the average consumption per kilometer of all trips and the total PV energy injected into the battery, we can estimate that the PV electricity would be enough to travel around 530 km. That distance is 30% of the total distance, 1750 km, covered during the measurement period. That is a good amount of range extension made possible by the onboard PV system.

However, there are significant caveats to the reported numbers. The measurements were carried out mainly during the summer when days are longer and mostly clear for the chosen location. because only one irradiance sensor was facing each side, mismatch losses within the module due to light inhomogeneity are not reported here. Furthermore, the measurement was carried out such that the vehicle was optimally parked for the best possible orientation with respect to the Sun. Parking time constitutes 93% of the measurement time, which might not necessarily correspond to the actual operation of a commercial vehicle whose majority of time is spent moving during the day-time. Nevertheless, the efficiency and energy yield numbers reported here provide a reasonable estimate of the functioning of a vehicle onboard PV system.

# 5 | Conclusion

We presented data analysis results of a vehicle onboard PV system with 15 modules connected to 10 MPPTs supplying power to the HV battery of a light commercial vehicle via an LV buffer battery and a DC-DC converter. The modules were added to the vehicle's roof, rear, left, and right sides, with irradiance sensors facing the same sides, along with necessary weather data measurement sensors. The data used in this analysis were collected from April to July 2021 for parking state at two locations, namely, ISFH and home, and trips between them. The collected data were processed and filtered, resulting in around 520 h of monitoring data for further analysis. The monitoring data were available for all the system's components, which enabled component-level energy flow analysis and overall energy

flow analysis represented as Sankey diagrams. The collected combined POA irradiation at ISFH, home parking locations, and trips was 305.5, 967.62, and 54.4 kWh after 106.7, 382.22, and 31.99h of operation, respectively. The combined modules converted irradiation on average with an 18% efficiency at both locations and trips. The MPPTs connected to the Sun-facing side and individual modules rather than modules connected in a series worked more efficiently. Overall, the roof-mounted modules produced the majority of the electricity for the parking locations and the trips. The DC-DC converter worked consistently at 90% efficiency for parking and trips, as it was independent of the weather fluctuations due to an LV buffer battery in the system architecture. The usable energy transferred to the HV battery was 29.65 and 99.74 kWh, respectively, for the ISFH and home parking locations, with an overall system efficiency of 60% and 65%. The average electricity consumption during the trips was 244Wh/km, considering the PV electricity generated during trips. With the approximately 129.39 kWh of electricity generated by the PV system at the two parking locations, a potential range extension of approximately 530 km was enabled. This accounts for 30% of the distance covered during the measurement period. The numbers presented here correspond to measurement scenarios with the vehicle being parked most of the time during the summer months and with optimal orientation with respect to the Sun. However, the numbers are a good reference for the efficiency of such systems and provide insight into how each component operates in such a PV application.

#### **Author Contributions**

Neel Patel: conceptualization (lead), software (equal), writing – original draft (lead), writing – review and editing (equal). Evgenii Sovetkin: software (equal), writing – review and editing (equal). Bart Pieters: software (equal), writing – review and editing (equal). Karsten Bittkau: writing – review and editing (equal). Kaining Ding: funding acquisition (lead). Robby Peibst: data acquisition, writing – review and editing (equal). Hilke Fischer: data acquisition. Angèle Reinders: writing – review and editing (equal).

# Acknowledgements

We want to thank our street project partners: Leibniz University of Hannover, a2-solar, Meyer-Burger, Vitesco, Continental Engineering Services, HZB Berlin, and the German Ministry for Economic Affairs and Energy for providing the funding as a part of the Street Project (FKZ 0324275). The authors gratefully acknowledge the Gauss Centre for Supercomputing e.V. (www.gauss-centre.eu) for funding this project by providing computing time through the John von Neumann Institute for Computing (NIC) on the GCS Supercomputer JUWELS at Jülich Supercomputing Centre (JSC). Open Access funding enabled and organized by Projekt DEAL.

#### **Data Availability Statement**

Research data are not shared.

#### References

1. A. Sierra Rodriguez, T. Santana, I. MacGill, N. J. Ekins-Daukes, and A. Reinders, "A Feasibility Study of Solar PV-Powered Electric Cars Using an Interdisciplinary Modeling Approach for the Electricity Balance,  $\mathrm{CO}_2$  Emissions, and Economic Aspects: The Cases of the Netherlands, Norway, Brazil, and Australia," *Progress in Photovoltaics*:

Research and Applications 28, no. 6 (2020): 517–532, https://doi.org/10. 1002/pip.3202.

- 2. Y. Ota, K. Araki, A. Nagaoka, and K. Nishioka, "Curve Correction of Vehicle-Integrated Photovoltaics Using Statistics on Commercial car Bodies," *Progress in Photovoltaics: Research and Applications* 30, no. 2 (2022): 152–163, https://doi.org/10.1002/pip.3473.
- 3. S. N. Mont, M. Heinrich, A. Pfreundt, C. Kutter, A. Tummalieh, and H. Neuhaus, "Energy Yield Modelling of 2D and 3D Curved Photovoltaic Modules," (2020): 6. Presented at the 37th EUPVSEC, [Online], https://www.eupvsec-planner.com/presentations/c50125/energy\_yield\_simulation\_of\_3d\_curved\_vipv\_modules.htm.
- 4. N. Patel, K. Bittkau, B. Pieters, E. Sovetkin, K. Ding, and A. Reinders, "Impact of Additional PV Weight on the Energy Consumption of Electric Vehicles With Onboard PV," (2023), https://doi.org/10.36227/techrxiv.22035002.v1.
- 5. P. Arun and S. Mohanrajan, "Effect of Partial Shading on Vehicle Integrated PV System," in 2019 3rd International Conference on Electronics, Communication and Aerospace Technology (ICECA), (Coimbatore, India: IEEE, 2019): 1262–1267, https://doi.org/10.1109/ICECA.2019.8821888.
- 6. M. Kolhe, S. K. Adhikari, and T. Muneer, "Parked Electric car's Cabin Heat Management Using Photovoltaic Powered Ventilation System," *Applied Energy* 233–234 (2019): 403–411, https://doi.org/10.1016/j.apenergy.2018.10.012.
- 7. A. Kouzelis, "Model-Based Impact Analysis of Vehicle-Integrated Photovoltaics and Vehicle-To-Grid on Electric Vehicle Battery Life," (2022), Accessed: Oct. 01, 2024. TU Delft, [Online], http://resolver.tudelft.nl/uuid:f3f716b3-f57e-486b-b5b9-8d5edf643d41.
- 8. C. Thiel, A. Gracia Amillo, A. Tansini, et al., "Impact of Climatic Conditions on Prospects for Integrated Photovoltaics in Electric Vehicles," *Renewable and Sustainable Energy Reviews* 158 (2022): 112109, https://doi.org/10.1016/j.rser.2022.112109.
- 9. M. Centeno Brito, T. Santos, F. Moura, D. Pera, and J. Rocha, "Urban Solar Potential for Vehicle Integrated Photovoltaics," *Transportation Research Part D: Transport and Environment* 94 (2021): 102810, https://doi.org/10.1016/j.trd.2021.102810.
- 10. M. C. Brito, R. Amaro, E. Silva, D. Pera, I. Costa, and D. Boutov, "Effect of Urban Shadowing on the Potential of Solar-Powered Vehicles," *Progress in Photovoltaics: Research and Applications* 32, no. 2 (2024): 73–83, https://doi.org/10.1002/pip.3737.
- 11. D. de Jong and H. Ziar, "Photovoltaic Potential of the Dutch Inland Shipping Fleet: An Experimentally Validated Method to Simulate the Power Series From Vessel-Integrated Photovoltaics," *Solar RRL* 7 (2022): 2200642, https://doi.org/10.1002/solr.202200642.
- 12. K. Araki, Y. Ota, and M. Yamaguchi, "Measurement and Modeling of 3D Solar Irradiance for Vehicle-Integrated Photovoltaic," *Applied Sciences* 10, no. 3 (2020): 872, https://doi.org/10.3390/app10030872.
- 13. E. Sovetkin, J. Noll, N. Patel, A. Gerber, and B. E. Pieters, "Vehicle-Integrated Photovoltaics Irradiation Modeling Using Aerial-Based LIDAR Data and Validation With Trip Measurements," *Solar RRL* 7 (2022): 2200593, https://doi.org/10.1002/solr.202200593.
- 14. PV2Go, Accessed: Oct. 08, 2022. [Online], https://pv2go.org/.
- 15. Y. Ota, K. Araki, A. Nagaoka, and K. Nishioka, "Evaluating the Output of a Car-Mounted Photovoltaic Module Under Driving Conditions," *IEEE Journal of Photovoltaics* 11, no. 5 (2021): 1299–1304, https://doi.org/10.1109/JPHOTOV.2021.3087748.
- 16. G. Wetzel, L. Salomon, J. Krügener, D. Bredemeier, and R. Peibst, "High Time Resolution Measurement of Solar Irradiance Onto Driving car Body for Vehicle Integrated Photovoltaics," *Progress in Photovoltaics: Research and Applications* 30 (2021): pip.3526, https://doi.org/10.1002/pip.3526.

- 17. V. Sionti, "Photovoltaic Potential of the Fleet of Urban Vehicles," (2021), accessed: Oct. 01, 2024. TU Delft, [Online], http://resolver.tudel ft.nl/uuid:66efa72e-51b9-43b7-ae9e-d9bf9b797261.
- 18. M. Wendeker, M. J. Gęca, Ł. Grabowski, K. Pietrykowski, and N. Kasianantham, "Measurements and Analysis of a Solar-Assisted City Bus With a Diesel Engine," *Applied Energy* 309 (2022): 118439, https://doi.org/10.1016/j.apenergy.2021.118439.
- 19. F. Karoui, B. Chambion, F. Claudon, and B. Commault, "Integrated Photovoltaics Potential for Passenger Cars: A Focus on the Sensitivity to Electrical Architecture Losses," *Applied Sciences* 13, no. 14 (2023): 8373, https://doi.org/10.3390/app13148373.
- 20. F. Karoui, F. Claudon, B. Chambion, S. Catellani, and B. Commault, "Estimation of Integrated Photovoltaics Potential for Solar City Bus in Different Climate Conditions in Europe," *Journal of Physics Conference Series* 2454, no. 1 (2023): 012007, https://doi.org/10.1088/1742-6596/2454/1/012007.
- 21. Lade-PV, accessed: Oct. 08, 2022. [Online], https://www.ise.fraunhofer.de/en/research-projects/lade-pv.html.
- 22. R. Peibst, H. Fischer, M. Brunner, et al., "Demonstration of Feeding Vehicle-Integrated Photovoltaic-Converted Energy Into the High-Voltage On-Board Network of Practical Light Commercial Vehicles for Range Extension," *Solar RRL* 6, no. 5 (2021): 2100516, https://doi.org/10.1002/solr.202100516.
- 23. Lightyear, [Online] https://lightyear.one/lightyear-0.
- 24. Sono Motors, [Online] https://sonomotors.com/.
- 25. IM Efficiency, [Online] https://imefficiency.com/index.
- 26. Copernicus Open Access Hub, [Online] scihub.copernicus.eu.
- 27. P. Fu and P. M. Rich, "Design and Implementation of the Solar Analyst: An ArcView Extension for Modeling Solar Radiation at Landscape Scales," in Proceedings of the 19th Annual ESRI User Conference, (1999).
- 28. R. Perez, R. Seals, and J. Michalsky, "All-Weather Model for Sky Luminance Distribution—Preliminary Configuration and Validation," *Solar Energy* 50, no. 3 (1993): 235–245.
- 29. GRASS r.sun, (2022). [Online], https://grass.osgeo.org/grass82/manuals/r.sun.html.
- 30. W. F. Holmgren, C. W. Hansen, and M. A. Mikofski, "pvlib Python: A python Package for Modeling Solar Energy Systems," *Journal of Open Source Software* 3, no. 29 (2018): 884, https://doi.org/10.21105/joss.00884.
- 31. PVsyst Help, "Albedo coefficient," [Online], https://www.pvsyst.com/help/albedo.htm.
- 32. E. Sovetkin M. Gordon, N. Patel, et al., "Non-Uniformity of Irradiation Distribution on Vehicles' Bodies," (2024): https://doi.org/10.22541/au.172114508.82017107/v1.
- 33. CAMS Radiation Service, [Online], https://www.soda-pro.com/web-services/radiation/cams-radiation-service.
- 34. B. Pieters, E. Sovetkin, and M. Gordon, "SSDP: Simple Sky Dome Projector," (2023). [Online]. github.com/IEK-5/SSDP.